Mesoporous ZnO nanoparticles using gelatin - Pluronic F127 as a double colloidal system for methylene blue photodegradation

Didik Prasetyoko*,†, Novia Amalia Sholeha**, Riki Subagyo*, Maria Ulfa***, Hasliza Bahruji****, Holilah Holilah*, Mokhammad Fajar Pradipta*****, and Aishah Abdul Jalil******,*******

*Department of Chemistry, Faculty of Science and Data Analytics, Institut Teknologi Sepuluh Nopember,
Keputih, Sukolilo, Surabaya, 60111, Indonesia
**College of Vocational Studies, Bogor Agricultural University (IPB University), Jalan Kumbang No. 14, Bogor 16151, Indonesia
***Study Program of Chemistry Education, Faculty of Teacher Training and Education, Universitas Sebelas Maret,
Jl. Ir. Sutami 36A, 57126 Surakarta, Central Java, Indonesia
****Centre for Advanced Materials and Energy Sciences, Universiti Brunei Darussalam,
Jalan Tungku Link, Gadong BE1410, Brunei Darussalam
*****Department of Chemistry, Faculty of Mathematics and Natural Sciences, Universitas Gadjah Mada,
Jl. Sekip Jogja, Central of Java, Indonesia
******Department of Chemical Engineering, Faculty of Chemical and Energy Engineering,
Universiti Teknologi Malaysia, 81310 UTM, Skudai, Johor Bahru, Johor, Malaysia
*******Centre of Hydrogen Energy, Institute of Future Energy, Universiti Teknologi Malaysia,
Skudai, 81310 UTM, Skudai, Johor Bahru, Johor, Malaysia
(*Received 4 March 2022 • Revised 22 June 2022 • Accepted 4 July 2022*)

Abstract−ZnO nanoparticles with mesopores enhanced the photocatalytic degradation of dyes. The potential of gelatin-Pluronic F127 as a double colloidal system was investigated for constructing mesoporosity in ZnO nanoparticles. Amphoteric gelatin with hydrophobic and hydrophilic tails formed a stable colloid as the surface-active agent. The studies highlighted the effect of different zinc precursors (zinc acetate, zinc sulphate and zinc nitrate) on ZnO formation and methylene blue (MB) degradation activity. Porous ZnO nanoparticles with uniform hexagonal structures were formed when zinc acetate exhibited a higher photocatalytic activity. Unprecedented $ZnSO_4$ resembling gunningite mineral was produced following high temperature calcination when using zinc sulfate as a precursor. The effect of temperature and concentration of MB solution indicated photodegradation reaction undergoes the first-order kinetic model. The mechanism of photocatalytic degradation of MB was determined using different types of scavenger agents, which indicated that hydroxyl radicals catalyzed the reaction.

Keywords: Zinc Oxide, Photocatalysis, Gelatin, Precursor

INTRODUCTION

Rapid production of synthetic dyes for textile and pharmaceutical industries has increased water pollution when dyes are discharged into the water without treatment [1,2]. Dye in wastewater can be removed by using membrane separation [3-5], biodegradation [6,7], physical adsorption [8,9], and photocatalysis [10,11]. Photocatalytic degradation of dye is a clean process requiring low energy consumption to remove wastewater pollutants but providing a high oxidation capacity [12,13]. The utilization of photon energy from sunlight for dye degradation has received wide attention due to the efficiency and the facile process while generating no secondary pollutants. The activity of photocatalysts strongly relies on their electronic properties for harvesting photon energy from sunlight to generate energy carriers. Apart from that, the syn-thesis of a nanoparticle photocatalyst with uniform morphology reduces structural defects that can act as recombination centers. Reducing the size of the photocatalyst also shortens the path for electron-hole migration to the surface.

ZnO has been applied in a wide range of applications, such as UV-photodetector, photocatalysis, optoelectronic devices, and gas sensors [14,15]. Zinc oxide (ZnO) generally exists as a hexagonal wurtzite structure with a direct band gap of ~3.37 eV and a high excitonic binding energy of 60 meV [16,17]. ZnO mitigates environmental pollution as a photocatalyst, especially for removing organic dyes from water and water splitting reactions. However, ZnO activity is restricted by its wide optical band gap that only absorbs photons in the UV region. Furthermore, ZnO experienced photo-stimulated corrosion at high pH, generating an inert $Zn(OH)_2$ structure. $Zn(OH)_2$ induced rapid electron and hole recombination, preventing charge carrier migration to the surface [18-21]. Continuous effort to enhance ZnO photocatalytic activity has focused on improving ZnO structural properties through its preparation method.

ZnO nanoparticles can be synthesized using sol-gel method,

hydrothermal process, thermal decomposition, chemical vapor deposition, and mechanochemical processes. ZnO is also produced via microemulsion synthesis in the presence of plant extracts such as B. retusa leaf or Peltophorum pterocarpum pod [22-24]. The hydrothermal method by self-assembly is gaining interest due to the ability to control structural properties and produce a high crystallinity and purity while employing inexpensive and simple lab equipment [25]. Self-assembly synthesis using the soft templating method is based on the formation of colloidal gel as a structure controlling agent [26-28]. In self-assembly synthesis, molecular arrangement occurs at the microscopic level to control nanoparticle growth. Pluronic (F127) is a triblock copolymer utilized as a soft template for targeting metallic precursors. F127 provides a simultaneous reduction and activation for directing the particle growth while restricting the dimensions of the particles. However, micelle stabilized by Pluronic F127 is unable to retain uniform morphology, mainly when the synthesis requires a high temperature calcination. The nanoparticles synthesized using the template Pluronic F127 are often calcined at 350 °C [29,30]. The combination of gelatin as a natural amphoteric template with F127 has been investigated to synthesize mesoporous carbon structures and hematite with flake-like morphology [31]. Gelatin is an exciting material to be used as a natural template since it is biodegradable, non-toxic, and extracted from abundant animal waste. Importantly, gelatin has amphoteric properties originating from -NH$_2$ and -C=O for interaction with the metallic ion. The presence of hydrophobic and hydrophilic tails in gelatin enhanced the stability of F127 for controlling the morphology even after high temperature calcination [31]. The synthesis of ZnO using gelatin as a soft template has been reported by Fang et al. The role of gelatin was to direct the self-assembly of nanorods ZnO clusters into star-like nanostructures [32].

Although gelatin can control ZnO morphology, the negative charge from carboxylic groups and the positive charge from amino groups can cause multiple metallic ion interactions via coordination or electrostatic interactions [33]. Interaction between the -NH$_2$ functionality in gelatin with the -OH group in F127 improved hybrid templates' stability while simultaneously eliminating multiple interactions with metal precursors. Double-colloidal synthesis was performed using zinc acetate, zinc nitrate, and zinc sulphate as Zn^{2+} ion sources. Different Zn^{2+} precursors show the importance of Zn-gelatin-F127 interaction during the crystallization process in controlling photoactivity. The morphology and the physicochemical properties of the resulting nanoparticles were investigated as photocatalysts for methylene blue degradation under UV-LED irradiation. UV-LED irradiation is used as the energy source based on its non-toxic, cheap, durable, and requiring less energy consumption. Photocatalytic activity is also determined under natural sunlight for the degradation of MB. Methylene blue (MB) is used based on its stability as an organic dye and is widely used coloring agent in the textile industry. In addition, MB is carcinogenic and mutagenic in the human body.

EXPERIMENTAL

1. Material

Block copolymer PEG-Pei-block (Pluronic F127), gelatin (pure

analysis, weighed molecule 5800, Sigma Aldrich), Ethanol (analytical grade), zinc sulphate trihydrate (Zn(SO$_4$)$_2$·3H$_2$O, Merck), zinc acetate dihydrate (Zn(CH$_3$COO)$_2$·2H$_2$O, Merck), zinc nitrate hexahydrate (Zn(NO$_3$)$_2$·6H$_2$O, Merck), sulfuric acid, (H$_2$SO$_4$, 100%, Sigma), HCl (37%, Sigma Aldrich).

2. Synthesis of Mesoporous ZnO

ZnO was synthesized by gradually dropping the water/ethanol solution (water : ethanol=1 : 3) into the Pluronic F127 solution using a burette (1 drop per 20 seconds) at room temperature. The mixture was then mixed with 1 M HCl and stirred in a closed container for 4 h at 150 rpm to prevent evaporation. Gelatin powder was added to the mixture and stirred for another 60 minutes. ZnSO$_4$ solution was gradually poured into the mixture from a burette at 1 drop for every 10 minutes at ambient conditions. The mixture was stirred continuously for 20 h at 150 rpm in a closed container. The mixture was transferred into a Teflon-lined hydrothermal reactor and heated at 100 °C for 24 h. The white solid was filtered and washed with distilled water until the pH of the supernatant was neutral. The solid was dried at 100 °C for 24 hours and then calcined at 550 °C for 6 hours. The ratio of ethanol : gelatin : F127 : Zn precursor : HCl was maintained at 125v : 0.12w : 12w : 27w : 0.001v. The ZnO samples were labeled based on the zinc precursor used in the synthesis; ZS for ZnSO$_4$, ZA for Zn(Ac)$_2$, and ZN for Zn(NO$_3$)$_2$.

3. Characterization

X-ray diffraction (XRD) characterization was evaluated to determine the crystallinity and phase of the synthesized ZnO by D5000 X-ray diffractometer (Siemens, Germany) using Cu Kα exciting source (λ=1.54056 Å). Fourier transform infrared (FTIR) analysis was carried out using a Bruker-Tensor 27 FTIR spectrometer (Germany). The porosity and surface area were determined using Brunauer-Emmett-Teller (BET) by Nova analyzer (Particle Test Pty Ltd, Bel Inc., Japan) using N$_2$ adsorption/desorption isotherms at 77 K in a liquid nitrogen media. Differential scanning calorimetry-thermal gravimetric analysis (DSC-TGA) (Thermoanalyzer Setaram model LABSYS^{tm} TG-DTA/DSC) was used to determine ZnO thermal properties. ZnO morphology was measured using JEOL transmission electron spectroscope (TEM, JEM-2100F, 120 KV) and scanning electron microscope- EDX (SEM-EDX, Shimadzu1350).

4. Photocatalytic Test

A homemade degradation reactor was used to assess 10 mL of MB solution (20 ppm) in a photocatalytic system with 0.005 g of ZnO in the laboratory scale. The reactor was constituted of a hotplate, a 50-mL glass, and a UV-LED strip. The UV-LED strip was composed of twelve lamps powered by EPILEDs (wavelength emission of 365 nm; power of 3 W/m) and equipped with automatic cooling in the lamp's surroundings. The photocatalytic test lasted 2 hours. The MB concentration was measured every 15 minutes using a UV-Vis Spectrophotometer (Genesys-10 UV-Vis) at a maximum wavelength of 664 nm.

RESULTS AND DISCUSSION

1. Catalyst Preparation

The crystallinity and structural phase of solid obtained from zinc nitrate (ZN), zinc acetate (ZA), and zinc sulfate (ZS) precursors were analyzed using the X-ray diffraction (XRD) method (Fig. 1). ZN
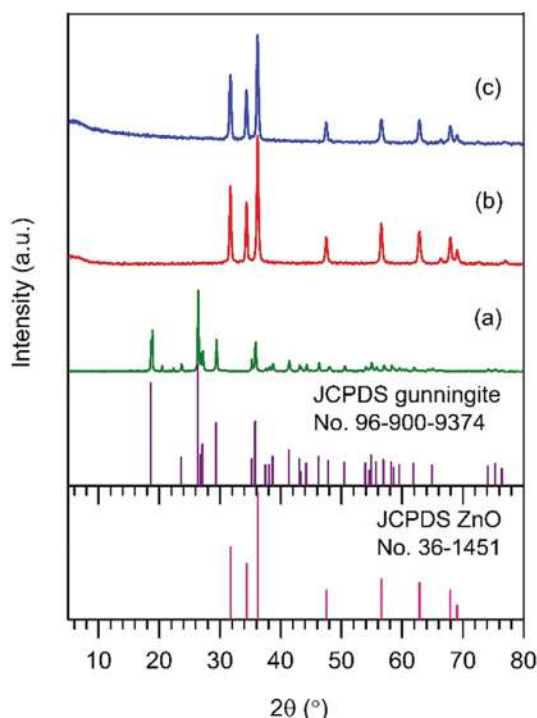
Fig. 1. XRD patterns of (a) ZnO from zinc sulfate precursor, ZS;
(b) ZnO from zinc acetate precursor, ZA; and (c) ZnO from
zinc nitrate precursor, ZN.

Fig. 2. FTIR spectra of (a) ZS, (b) ZA, and (c) ZN.

and ZA showed the main peaks corresponding to ZnO at $2\theta=$ 31.76, 34.41, 36.24, 47.52, 56.58, 62.84, 67.93, and 69.07°. There was a slight increase in intensity when ZnO was synthesized from zinc acetate precursor compared to zinc nitrate. Nevertheless, no evidence of impurities was observed, suggesting calcination at 500 °C removed carbon species from the decomposition of gelatin and F127 template. Amorphous carbon generally appeared as a broad hump centered at 24°. ZnO synthesized from zinc sulfate showed the main peaks at $2\theta=$18.86°, 26.41°, 27.12°, 29.46°, 35.86°, 41.34°, 43.05°, 46.23°, 50.47°, 53.95°, 54.90° and 56.92°, indicating the formation of gunningite crystal, which is a stable phase of hydrated $ZnSO_4$ [34]. Note that the calcination temperature was enhanced to 500 °C to promote ZnO formation; however, there is no evidence of ZnO characteristic peaks from the XRD of the ZS sample. The XRD results provide information on the importance of the counter anion of Zn precursor during the synthesis of ZnO in a colloidal system. Hydrolysis of zinc sulfate produced zinc hydroxide ($ZnOH^-$) species, which subsequently transformed into ZnO. However, the sulfate anion transformed a mixture of F127 and gelatin to form a stable sulfate anion surfactant, allowing the self-assembly of $ZnOH^-$ species to generate a highly crystalline layered structure.

Lattice parameters of ZnO were determined using the Bragg equation followed by hexagonal system equation of ZnO. The a and c values of ZA were calculated at 3.255 Å and 5.218 Å, respectively; meanwhile, the a=3.252 Å and c=5.224 Å were determined from ZN. In comparison to the standard ZnO lattice parameter by JCPDS 36-1451 (a=3.249 Å, c=5.207 Å), the a and c values were slightly higher, suggesting the synthesis methods and the experimental conditions, such as template, temperature, heating rate, reac-
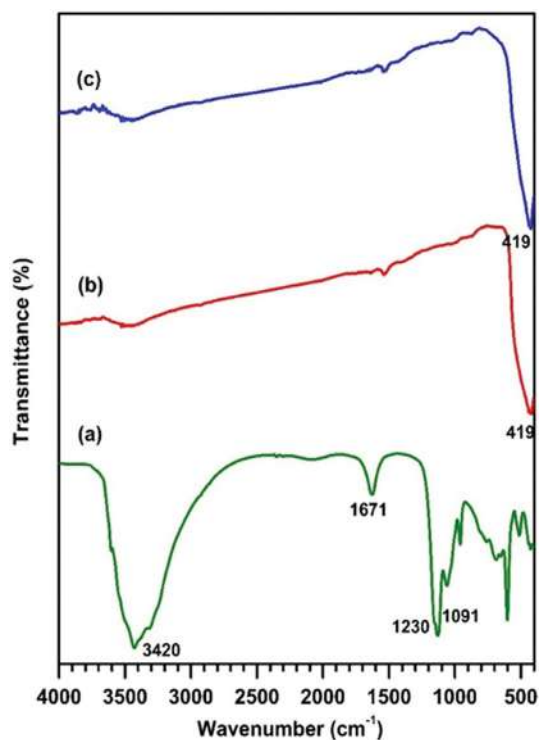
tion time, and solvent generated different levels of long-range structural organization of hexagonal lattice. However, the ZS lattice parameter could not be determined due to the absence of ZnO diffraction peak.

FTIR analysis was performed to determine the functional group of ZnO synthesized from the gelatin-F127 template (Fig. 2). ZnO derived from zinc acetate (ZA) and zinc nitrate (ZN) as precursors showed similar absorption bands at 3,420 cm^{-1} and 419 cm^{-1}, which corresponded to the vibration of surface hydroxyl group/ physisorbed water and Zn-O bending vibration, respectively [35]. There are no other absorption bands that could indicate the presence of carbon impurities on the structure. Meanwhile, a powder sample obtained from zinc sulfate, as ZS precursor, revealed a broad absorption band at 3,420 cm^{-1} corresponding to hydroxyl group or water vibration. The band at 1,671 cm^{-1} was ascribed to H-O-H bending. Apart from that, the absorption bands at 1,230 cm^{-1} and 1,091 cm^{-1} corresponded to S=O asymmetric and symmetric stretches, respectively, which further proved the presence of sulfate anion on the structure [36]. The Zn-O bonds displayed a sharp peak at 505 cm^{-1}; meanwhile, the low absorption peak at 419 cm^{-1} in ZS indicated the bending vibration of Zn-O in zinc hydroxide salt.

Thermal properties of solid powder obtained after hydrothermal treatment were determined using TGA analysis. The analysis temperature was increased to 600 °C at 10 °C/min. Fig. 3 shows that the ZN and ZA experienced the first weight loss stage when annealed to 125 °C due to the desorption of physisorbed water. Removing chemically adsorbed water from 125 °C to 220 °C resulted in further weight loss [37]. ZnO from nitrate and acetate precursors experienced 55.2% and 40.1% of total weight loss from the
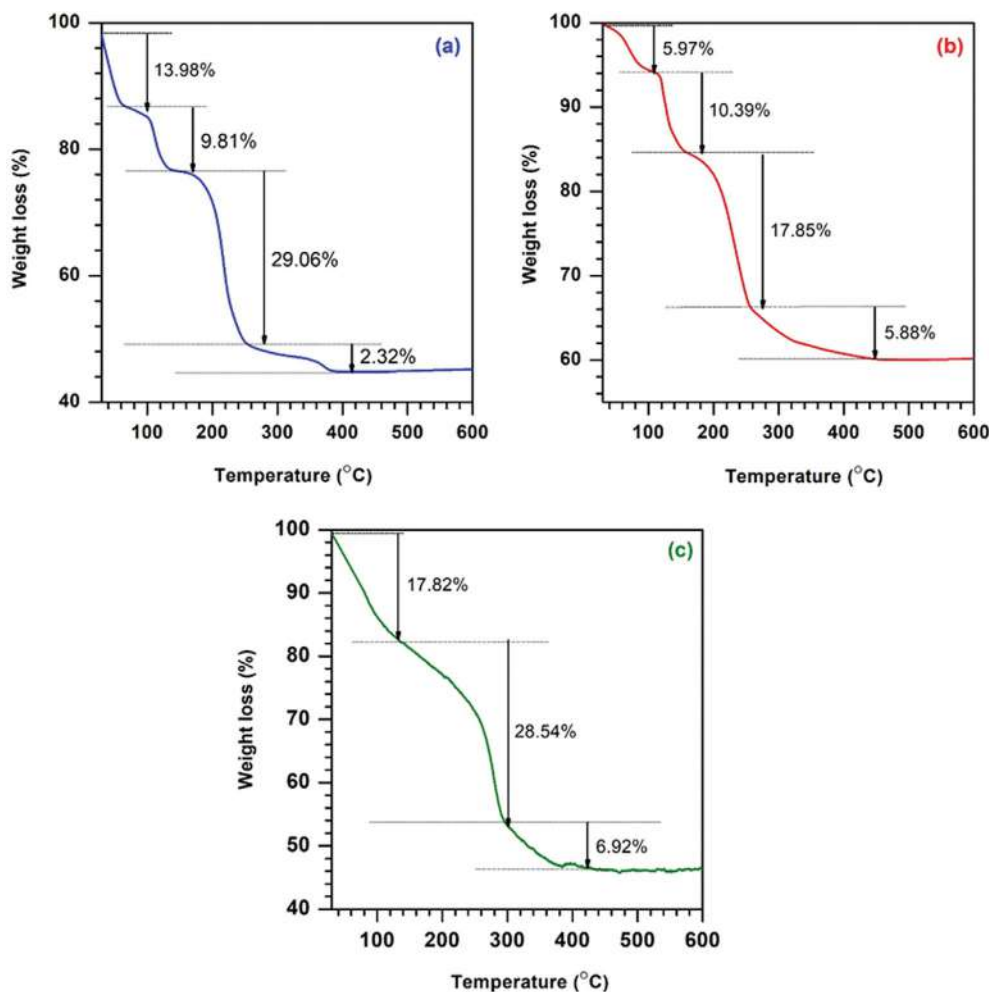
Fig. 3. TGA analysis of (a) ZA, (b) ZN and (c) ZS before calcination.

decomposition of residual organic molecules that are still present after calcination. Thermal decomposition profiles of powder samples obtained from ZS were slightly different than ZN and ZA. Three decomposition stages were observed on ZS, which involved gradual physisorbed water evacuation up to 120 °C. The ZS sample was further decomposed to show two more decomposition stages at 300 °C and 400 °C, presumably due to the decomposition of F123 and gelatin, respectively. The sample also experienced 53.3% total weight loss. Interestingly, the decomposition of dried powder obtained from zinc sulfate only showed three decomposition stages, whereas ZN and ZA revealed four decomposition stages. The observation indicates that the thermal stability of Zn-gelatin-F123 composites varied depending on the source of Zn^{2+} precursor.

TEM analysis of the samples after calcination at 500 °C is shown in Fig. 4. ZnO from zinc acetate formed nanoparticles with a well-defined hexagonal structure. The particle size was determined from multiple TEM images at ~15-85 nm. TEM analysis of ZnO obtained from zinc nitrate precursor showed the formation of spherical nanoparticles with an estimated particle size of 10-150 nm. The solid powder obtained from zinc sulphate (ZS) showed the formation of large aggregates with a non-uniform morphology. To further investigate the morphology of ZS, SEM analysis was carried out as displayed in Fig. 4(h). ZS was observed as an agglomeration of particles with a needle-like structure. The particle size of ZS was determined at approximately 1.5 μm.

The Brunauer-Emmett-Teller (BET) theory is well-known for analyzing textural properties such as surface area and pore volume. Fig. 5 represents the N_2 adsorption-desorption isotherms and Barrett-Joyner-Halenda (BJH) pore size distribution of as-prepared ZnO synthesized from different Zn precursors. According to IUPAC classification, all samples show Type IV isotherms with capillary condensation (H3 hysteresis loops) corresponding to mesoporous material [38]. At high P/P_0, the H3 loop does not show any limiting adsorption and is usually linked with the aggregated particles. The BJH method further indicates pore size distribution at 2.9-25 nm of ZnO particles based on the sharp inflection at a relative
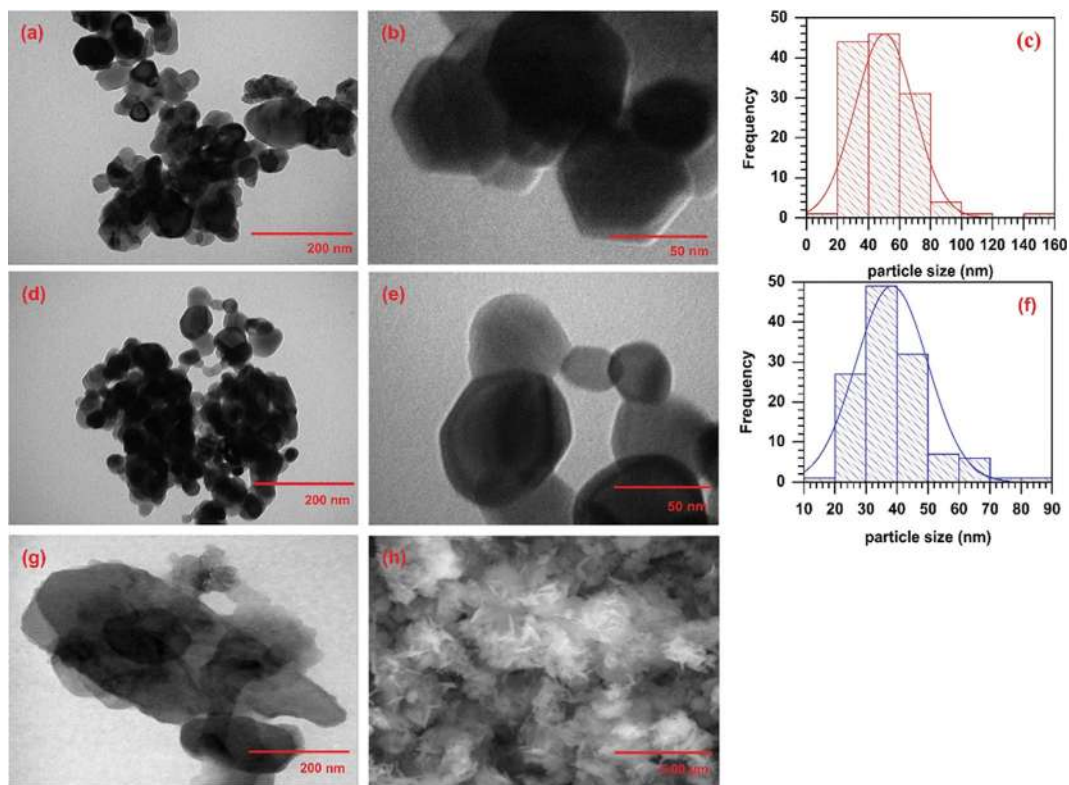
Table 1. Physicochemical properties

Samples	S_{BET} (m² g⁻¹)	V_{meso} (cm³ g⁻¹)	D_{meso} (nm)	Band gap (eV)
ZA	14.37	0.6724	25.108	3.06
ZN	5.28	0.0270	2.969	3.04
ZS	13.24	0.0479	14.452	-

Fig. 4. TEM analysis of (a), (b) ZA, (d), (e) ZN, and (g) ZS; Particle size distribution histogram of (c) ZA and (f) ZN; (h) SEM analysis of ZS.
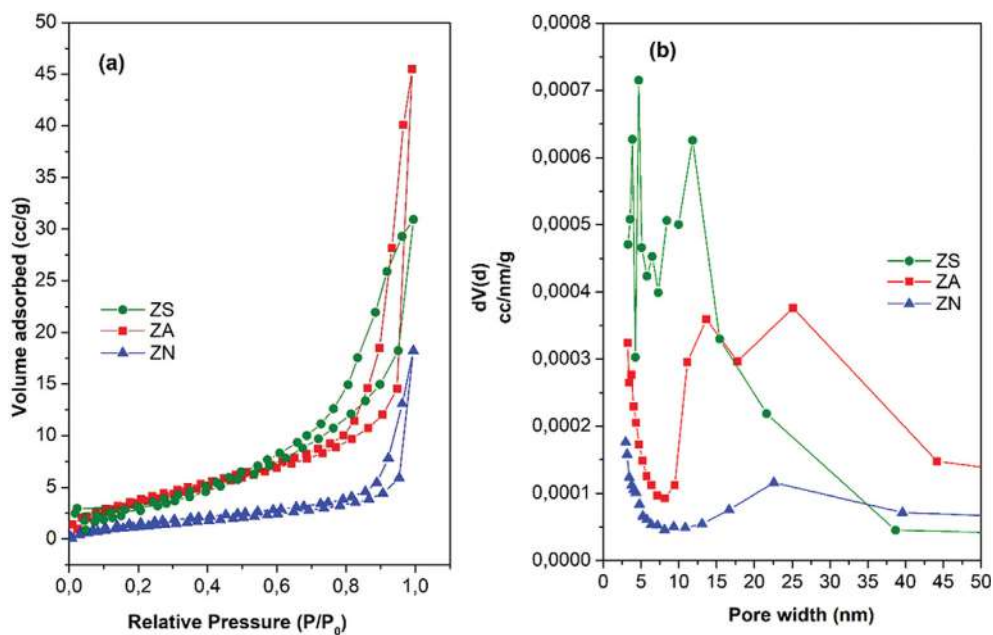

Fig. 5. The N- adsorption-desorption isotherms (a) and the pore size distribution (b) of ZS, ZA and ZN samples.

pressure of 0.5-0.8. The specific surface area of ZN, ZA, and ZS was determined at 14, 5, and 13 m^2 g^{-1}, respectively (Table 1). The specific surface area of ZnO obtained in this study was higher than the previously reported ZnO using the ultrasound method at 2.95-5.54 m^2/g [39].

Fig. 6 represents the UV-Vis spectra of ZnO from zinc nitrate

and zinc acetate precursors. Note that ZS shows no absorbance in the UV visible region. The absorption band resulted from the transition of electrons between the valence and conduction band. The presence of intrinsic defect levels can also contribute to the photo-adsorption properties of ZnO [40]. As shown in Fig. 5(a), the absorbance edges of ZA and ZN were observed at ~380 nm. ZnO
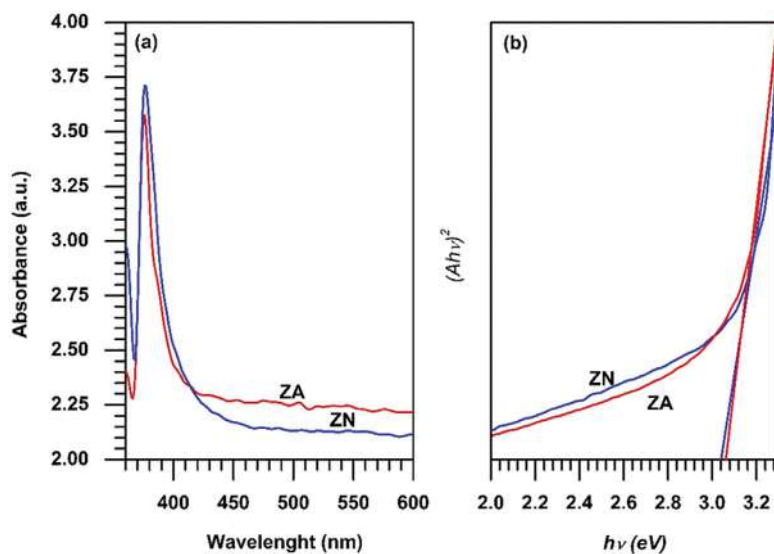
Fig. 6. (a) The absorption properties and (b) Tauc's plot of the as-prepared ZnO.
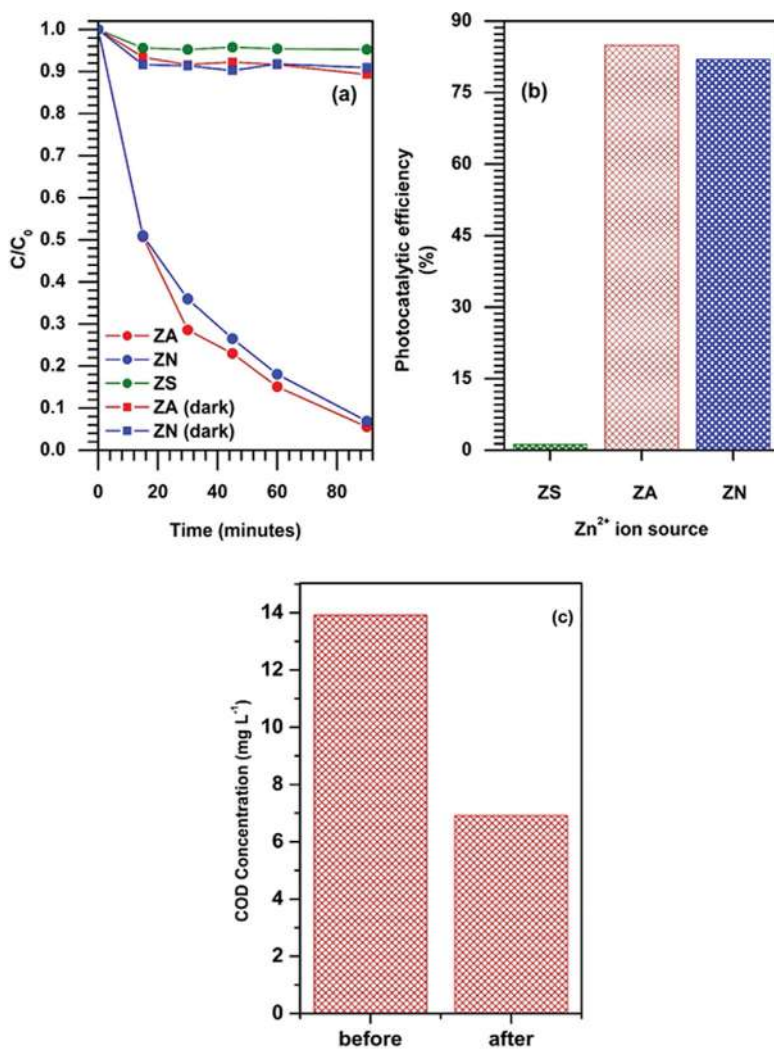

Fig. 7. Effect of Zn precursor in photocatalytic activity of ZnO towards MB degradation. (a) The plot of $C_{final, MB}$ versus irradiation times, (b) The percentage of photodegradation efficiency of ZnO produced from zinc nitrate (ZN), zinc acetate (ZA), and zinc sulfate (ZS), and (c) COD analysis before and after photodegradation process.

has an absorption edge at ~365 nm with a band gap energy of 3.4 eV. The band gap energy estimation of ZnO was calculated by Tauc's plot using Eq. (1):

$$\alpha h\nu = A(h\nu - E_g)^{1/2} \tag{1}$$

where α is the coefficient of absorption, A is a proportional constant, $h\nu$ is the energy of photons, and Eg is the bandgap energy. According to Fig. 5(b), the band gap energy values for ZN and ZA were estimated at 3.04 and 3.06 eV. The band gap energy was slightly reduced due to the optical confinement effect of small crystallites. In general, the band gap energy increased with the reduction of crystallite size [40,41]. Apart from that, the red shift of the band edge suggests the ZnO developed a shallow energy level near the valance band due to the presence of foreign atoms in the lattice. There is a possibility that the residual carbon impurities after calcination may be trapped in the ZnO lattice, responsible for the red shift [42].

2. Photocatalytic Activity

2-1. Effect of Precursor

The effect of zinc precursor on the activity of ZnO as a photocatalyst was investigated in photodegradation on MB. ZnO obtained from zinc acetate precursor (ZA) showed a slightly faster MB degradation than ZN, whereas ZS only removed a trace amount of MB in the solution (Fig. 7). The high surface area and mesopore volume of ZA may be responsible for increasing the adsorption of MB molecules on the surface during photocatalytic degradation. In addition, TEM analysis indicated that ZA has a larger nanoplate size, exposing {0001} facets. The high percentage of {0001} facets in photocatalyst nanoparticles increased the activity of chemisorbed oxygen species during aerobic photocatalytic reactions [43]. A highly active oxygen species on the ZnO surface increases the formation of hydroxyl radicals responsible for the photodegradation of MB. However, since ZnO was not formed when using zinc sulfate precursor, the slight removal of MB originated from the physical adsorption on the ZS surface. Experiments in dark conditions were carried out to confirm that photocatalytic degradation was responsible for MB removal using ZA and ZN. Reaction in dark conditions reached equilibrium at 15 minutes, with no significant changes in the MB concentration up to 90 min. Photocatalytic degradation was also conducted under direct sunlight with a UV index of 9 at 10 ppm of MB concentration. MB degradation was determined at 100% removal efficiency after 60 minutes when using ZA and ZN as photocatalysts, comparable with the UV LED light source activity.

The total mineralization of MB was determined through chemical oxygen demand (COD) analysis of the final filtrate after photodegradation. COD was used to evaluate the impact of pollutants on water quality [44]. COD analysis of the final solution provides information on the toxicity levels of the photodegradation products. A high level of COD in water indicates threats to human health. The initial COD value of MB solution was determined at 13.92 mg·L^{-1}. The COD value was significantly decreased at ~50% to give 6.96 mg·L^{-1} after illumination for 90 minutes (Fig. 7(c)). The result indicated that MB was degraded and mineralized using ZnO.

2-2. Effect of Temperature

The effect of temperature in the photodegradation of MB was investigated on ZnO from zinc acetate precursors at 30 °C, 40 °C, and 50 °C. Fig. 8 shows that the increase in temperatures slightly reduced degradation rates. Variation of temperature on the degradation rate is often associated with the increase in the kinetic energy of MB molecules in the solution. High kinetic energy increases diffusion, thus reducing the amount of adsorbed molecules on the surface [45]. The low amount of MB molecules adsorbed on the ZnO surface led to the recombination of hydroxyl radicals into water [46]. The first-order kinetic model was applied based on Eq. (2) to determine the photodegradation rate of MB. All the parameters of the first-order kinetic model are presented in Table 2.

$$\ln\frac{C}{C_0} = -kt \tag{2}$$

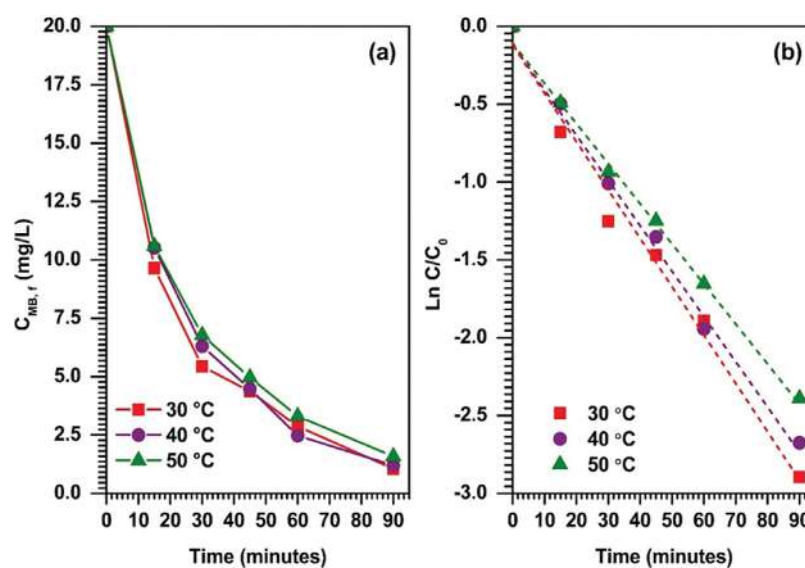where C and C_0 are final and initial MB concentration (mg L^{-1}),

Fig. 8. The effect of temperature of MB solution (a) in photocatalytic degradation over ZnO from zinc acetate (ZA) and (b) The plot of first-order kinetic model.
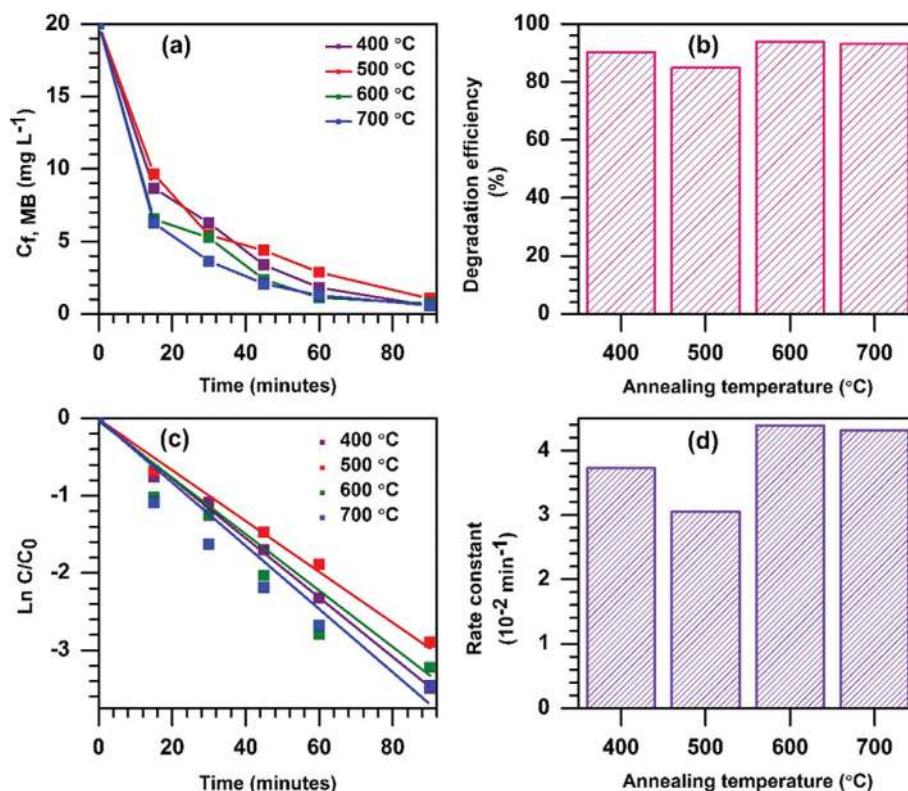
Fig. 9. Effect of annealing temperature of ZnO (ZA). (a) Plot of C_{final} over irradiation time, (b) photodegradation efficiency at irradiation time of 60 minutes, (c) first-order kinetic plot, and (d) rate constant at different annealing temperatures.

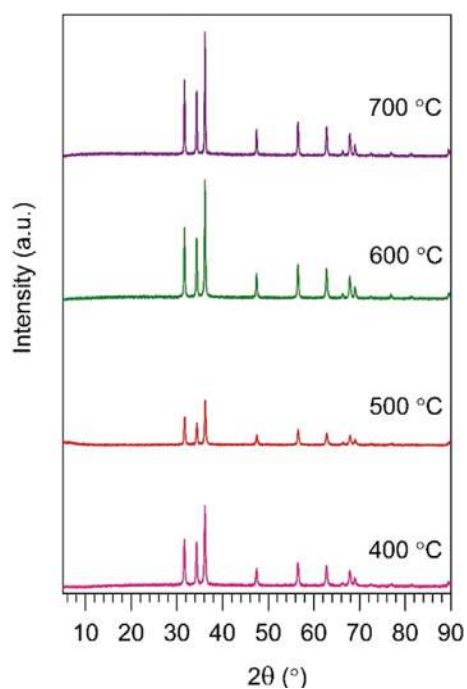respectively, k is the rate constant of reaction (min^{-1}), and t is irradiation time (min).

Fig. 10. XRD pattern of ZnO from zinc acetate at different of calcination temperatures.

2-3. The Effect of Annealing Temperature

The effect of annealing temperature was investigated on ZnO obtained from zinc acetate precursor after calcination at 400, 500, 600, and 700 °C in the air for 3 h. Fig. 9 shows calcination at 600 °C, and 700 °C increased the rate of photodegradation within the first 10 min into the reaction. These results show that a higher calcina-

Table 2. Parameter of first-order reaction in MB photocatalytic at different temperature

Temperature (°C)	Parameters		
	Correlation coefficient (R^2)	Rate constant (k, min^{-1})	Initial rate (r_0, mg L^{-1} min^{-1})
30	0.9928	0.0308	0.616
40	0.9975	0.0296	0.592
50	0.9962	0.0261	0.522

Table 3. Crystallinity and initial rate of photodegradation for ZnO after calcined at different temperatures

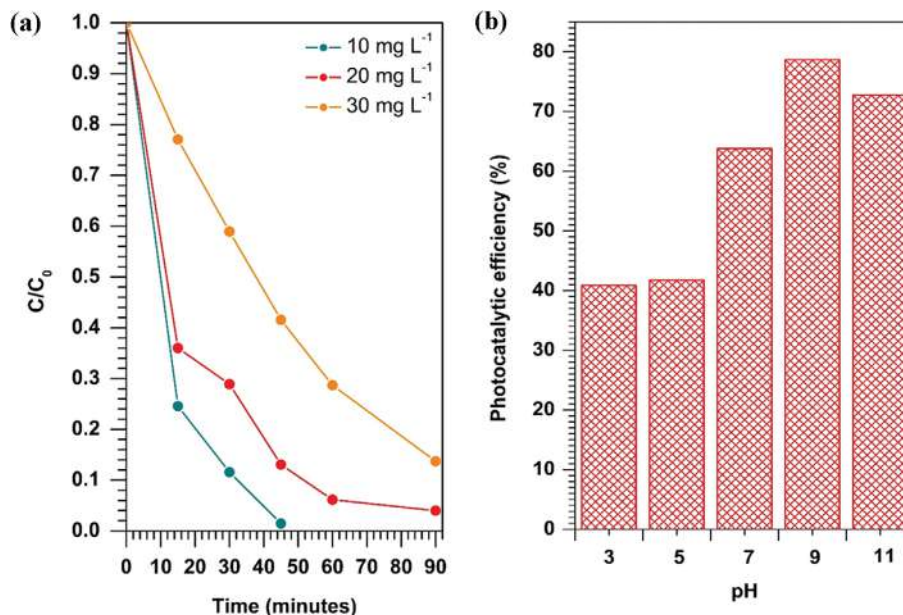| Annealing temperature (°C)	Crystallinity (%)	Initial rate ($10^{-1} \times$ M min^{-1})
400	63.76	7.62
500	36.06	6.1
600	92.88	8.78
700	100	8.62

Fig. 11. The effect of MB concentration (a) and pH of MB solution (b) on photodegradation efficiency of ZnO from zinc acetate.

tion temperature improves the crystallinity of ZA via the elimination of carbon impurities, as indicated by the XRD analysis in Fig. 10 and Table 3. Consequently, the lifetime of the photogenerated charge carrier was enhanced due to the elimination of the recombination center [47]. Kinetic analysis in Fig. 9(c) and 9(d) clearly shows that increasing the calcination temperature improves the kinetic and the rate of MB degradation.

2-4. Effect of MB Concentration and pH of Solution

The effect of MB concentration at 10, 20 and 30 mgL^{-1} on the efficiency of the photodegradation process indicates that the activity decreased with increasing of MB concentration (Fig. 11). It is postulated that at a higher MB concentration, the saturation of ZnO with MB molecules restricts photons' adsorption. The low number of adsorbed photons led to a reduction of hydroxyl radical formation. The result was further confirmed by the MB photocatalytic rate in Table 4. The highest photocatalytic activity at 10 mg L^{-1} suggests that the photodegradation on ZnO was favorable at low MB concentration.

The adsorption of MB molecules on ZnO depends on its surface properties, which can be improved with pH variation. An efficient photocatalytic process requires a significant accumulation of MB on the surface. The effect of pH solution on the degradation of MC was investigated by adding NaOH 0.5 M (basic) or HCl 0.5 M (acidic) to alter the interaction with the ZnO surface.

Table 4. Photodegradation at different initial concentrations of MB and first-order constant values for MB degradation using ZA

Initial conc. C_o (mg L^{-1})	Rate, k_{app} ($\times 10^{-2}$ min^{-1})	Initial rate, r_o ($\times 10^{-1}$ mg L^{-1} min^{-1})
10	8.94	8.94
20	4.39	8.78
30	2.08	6.24

The concentration of MB was reduced to 50 mg L^{-1} since almost 100% of removal was achieved at 20 mg L^{-1}. However, a similar amount of ZnO photocatalyst (5 mg) was used throughout the experiments. Fig. 11(b) shows that the photodegradation in the basic solution was higher than in the acidic condition, with the optimum photocatalytic rate obtained at pH 9. As a cationic dye, a higher interaction between MB and the negatively charged surface of ZnO was generated following the NaOH addition. In addition, the presence of excess OH$^-$ in the solution enhanced the trapping of electron and hole for •OH radical production, therefore increasing the photocatalytic oxidation [48].

2-5. Methylene Blue Photocatalytic Mechanism

The study reported the potential of gelatin and Pluronic F127 as organic templates for synthesizing mesoporous ZnO nanoparticles while using zinc nitrate and zinc acetate as the precursor. Calcination at 500 °C transformed the resulting powder into mesoporous nanoparticles with a well-defined hexagonal structure. The effect of zinc precursor on the formation of mesoporous ZnO nanoparticles showed that zinc sulfate failed to produce ZnO after calcination at 500 °C. Instead, the resulting powder is characterized as zinc sulfate mineral. Although the resulting powder is inactive for photocatalytic reactions, it is interesting to understand the effect of counter anion in ZnO formation. In general, calcination of zinc precursor at high temperatures transformed the hydrolyzed zinc into ZnO. The presence of gelatin increased F127 stability via interaction between amine groups in gelatin with the hydroxyl group in F127. The emulsion is stable enough to preserve the nanoparticle's structure even at high temperature calcination. The presence of sulfate transformed gelatin and F127 mixtures into a mixture of surfactants with sulfate anions, thus rearranging the stabilized Zn^{2+} into gunningite minerals.

Nevertheless, ZnO produced from zinc nitrate, and zinc acetate precursors exhibited photocatalytic activity for degradation of MB under UV LED and natural sunlight irradiation. The mechanism
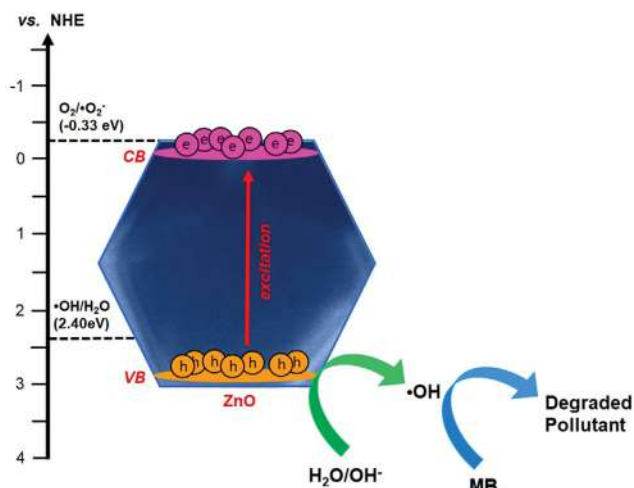
Fig. 12. **Proposed mechanism of methylene blue photocatalytic on ZnO under UV-LED irradiation.**

of MB photodegradation was proposed based on the determination of the charge transfer mechanism using the electronegativity concept in Eqs. (3) and (4) [48] in order to determine the band edge position of ZnO.

$$E_{VB} = X - E^e + \frac{1}{2}E_g \qquad (3)$$

$$E_{CB} = E_{VB} - E_g \qquad (4)$$

E_{VB} and E_{CB} are the VB and CB energy levels, respectively. E^e (~4.5 eV) is the energy of a free electron on the hydrogen scale. E_g is the band gap energy of semiconductor, and X indicates the semiconductor's electronegativity, which is determined by the mean of the electron affinity energy and first ionization. The X value for ZnO from zinc acetate was calculated as 5.76 eV. The calculated E_{VB} and E_{CB} of ZA are 2.79 and -0.27 eV, respectively.

Fig. 12 illustrates the band position and the proposed mechanism of MB degradation on a single ZnO during the photocatalytic reaction. When UV light penetrated the ZnO surface, the photon energy was utilized for electron excitation from VB to CB, leaving a hole on VB. Due to the potential of E_{CB} being higher compared to $O_2/\bullet O_2$ (~-0.33 for NHE), the reduction of O_2 to $\bullet O_2$ by the excited electron was impossible. However, the photogenerated h^+ in the valence band in ZnO was feasible to produce $\bullet OH$ radicals because the position of VB level is more positive than the potential level of $H_2O/\bullet OH$ (~2.27 eV for NHE) [49]. $\bullet OH$ radicals are very reactive oxidation species for the degradation of MB molecules. The photocatalytic degradation of MB is summarized as follows:

$$ZnO + h\upsilon \rightarrow ZnO\ (e^-_{CB} + h^+_{VB}) \qquad (5)$$

$$h^+_{VB} + H_2O \rightarrow HO\bullet + H^+ \qquad (6)$$

$$h^+_{VB} + OH^- \rightarrow \bullet OH \qquad (7)$$

$$MB + \bullet OH \rightarrow CO_2 + H_2O + \text{degradation products} \qquad (8)$$

Hydroxyl radical, $\bullet OH$ is a reactive radical species responsible for bond dissociation and oxidation, such as C-N=C fragments during
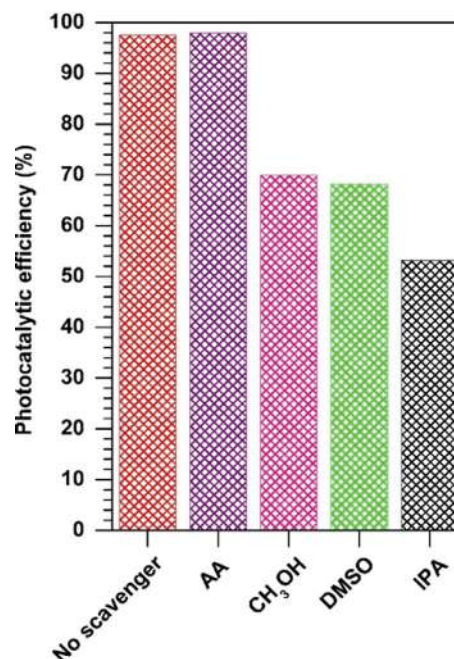

Fig. 13. **The efficiency of methylene blue photodegradation in the presence of scavenger agents using ZnO from zinc acetate precursor.**

MB photodegradation. The unsaturated C-C bond was dissociated by $\bullet OH$ radical [50,51] to form the intermediate species, subsequently oxidized to produce H_2O and CO_2.

The utilization of scavenger molecules was investigated to verify the active species during the MB photocatalytic process. Isopropanol (IPA) acted as hydroxyl radicals/$\bullet OH$ scavenger [52], meanwhile dimethyl sulfoxide (DMSO) was utilized as electron/e^- scavenger [53]. The addition of methanol (CH_3OH) in photocatalytic reaction will explain the role of photodegraded hole/h^+ in degradation reaction [54]. Meanwhile, ascorbic acid (AA) was utilized as a superoxide radical/$\bullet O_2^-$ scavenger. Fig. 13 shows that the addition of ascorbic acid to the catalyst suspension achieved similar photodegradation efficiency as the MB solution without the addition of a scavenger compound. These results verified that $\bullet O_2$ was inadequate to generate in the system due to the conduction band of ZnO being lower than $O_2/\bullet O_2^-$ potential. The addition of methanol and DMSO showed a reduction in photocatalytic efficiency to only ~68%. Meanwhile, when isopropyl alcohol was added, the efficiency dropped to only 52%, implying that $\bullet OH$ radicals largely catalyze photodegradation. However, since the hydroxyl radical can be generated via the reaction of an electron or hole with a surface hydroxyl group or water, the addition of electron and hole scavenger also reduced the photodegradation of MB.

CONCLUSION

We have developed a double colloidal system to prepare mesoporous ZnO nanoparticles using gelatin and Pluronic F127 templates and different types of Zn^{2+} precursors. Photodegradation of methylene showed high efficiency of photocatalysts obtained from zinc acetate (ZA) and zinc nitrate (ZN); meanwhile, utilization of

zinc sulfate (ZS) as precursor produced inactive catalysts. Characterization studies revealed that only zinc nitrate and zinc acetate produced ZnO; zinc sulfate formed a stable gunningite mineral. TGA analysis data suggested that the stable phase of zinc sulfate upon interaction with gelatin and pluronic prevented the transition into ZnO.

ACKNOWLEDGEMENTS

COMPETING INTERESTS

The authors declare no competing interests.

REFERENCES

1. C. A. Soto-Robles, O. Nava, L. Cornejo, E. Lugo-Medina, A. R. Vilchis-Nestor, A. Castro-Beltrán and P. A. Luque, *J. Mol. Struct.*, **1225**, 129101 (2021).
2. N. Belachew, M. H. Kahsay, A. Tadesse and K. Basavaiah, *J. Environ. Chem. Eng.*, **8**, 104106 (2020).
3. R. Molinari, C. Lavorato and P. Argurio, *Catal. Today*, **281**, 144 (2017).
4. S. Mozia, *Sep. Purif. Technol.*, **73**, 71 (2010).
5. S. Leong, A. Razmjou, K. Wang, K. Hapgood, X. Zhang and H. Wang, *J. Membr. Sci.*, **472**, 167 (2014).
6. R. K. Sonwani, G. Swain, B. S. Giri, R. S. Singh and B. N. Rai, *Bioresour. Technol.*, **302**, 122811 (2020).
7. H. Ali, *Water. Air. Soil Pollut.*, **213**, 251 (2010).
8. S. Moosavi, C. W. Lai, S. Gan, G. Zamiri, O. Akbarzadeh Pivehzhani and M. R. Johan, *ACS Omega*, **5**, 20684 (2020).
9. B. Acevedo, R. P. Rocha, M. F. R. Pereira, J. L. Figueiredo and C. Barriocanal, *J. Colloid Interface Sci.*, **459**, 189 (2015).
10. L. Bai, S. Li, Z. Ding and X. Wang, *Colloids Surf. A Physicochem. Eng. Asp.*, **607**, 125489 (2020).
11. J. Buasakun, P. Srilaoong, G. Chaloeipote, R. Rattanakram, C. Wongchoosuk and T. Duangthongyou, *J. Solid State Chem.*, **289**, 121494 (2020).
12. M. A. Rauf and S. S. Ashraf, *Chem. Eng. J.*, **151**, 10 (2009).
13. M. Rochkind, S. Pasternak and Y. Paz, *Molecules*, **20**, 88 (2014).
14. S. Hossain and D. M. Chun, *Mater. Chem. Phys.*, **255**, 123589 (2020).
15. P. Nandi and D. Das, *Appl. Surf. Sci.*, **465**, 546 (2019).
16. K. M. Lee, C. W. Lai, K. S. Ngai and J. C. Juan, *Water Res.*, **88**, 428 (2016).
17. K. Qi, B. Cheng, J. Yu and W. Ho, *J. Alloys Compd.*, **727**, 792 (2017).
18. X. Chen, Z. Wu, D. Liu and Z. Gao, *Nanoscale Res. Lett.*, **12**, 1 (2017).
19. M. Aqeel, M. Rashid, M. Ikram, A. Haider, S. Naz, J. Haider, A. Ul-Hamid and A. Shahzadi, *Dalt. Trans.*, **49**, 8314 (2020).
20. S. M. Mousavi, A. R. Mahjoub and R. Abazari, *J. Mol. Liq.*, **242**, 512 (2017).
21. M. Y. Guo, A. M. C. Ng, F. Liu, A. B. Djurišić, W. K. Chan, H. Su and K. S. Wong, *J. Phys. Chem. C*, **115**, 11095 (2011).
22. T. Gur, I. Meydan, H. Seckin, M. Bekmezci and F. Sen, *Environ. Res.*, **204**, 111897 (2022).
23. R. Vinayagam, S. Pai, T. Varadavenkatesan, A. Pugazhendhi and R. Selvaraj, *Appl. Nanosci.* (2021).
24. R. Vinayagam, S. Pai, G. Murugesan, T. Varadavenkatesan and R. Selvaraj, *Appl. Nanosci.* (2021).
25. Y. Y. Chan, Y. L. Pang, S. Lim and W. C. Chong, *J. Environ. Chem. Eng.*, **9**, 105417 (2021).
26. A. Goux, M. Etienne, E. Aubert, C. Lecomte, J. Ghanbaja and A. Walcarius, *Chem. Mater.*, **21**, 731 (2009).
27. A. Walcarius, E. Sibottier, M. Etienne and J. Ghanbaja, *Nat. Mater.*, **6**, 602 (2007).
28. C. Li, Q. Li, Y. V. Kaneti, D. Hou, Y. Yamauchi and Y. Mai, *Chem. Soc. Rev.*, **49**, 4681 (2020).
29. B. Deljoo, T. Jafari, R. Miao, M. P. Nieh, S. L. Suib and M. Aindow, *Mater. Des.*, **180**, 107902 (2019).
30. S. Kerkhofs, T. Willhammar, H. Van Den Noortgate, C. E. A. Kirschhock, E. Breynaert, G. Van Tendeloo, S. Bals and J. A. Martens, *Chem. Mater.*, **27**, 5161 (2015).
31. M. Ulfa, D. Prasetyoko, A. H. Mahadi and H. Bahruji, *Sci. Total Environ.*, **711**, 135066 (2020).
32. K. M. Fang, Z. Z. Wang, M. Zhang, A. J. Wang, Z. Y. Meng and J. J. Feng, *J. Colloid Interface Sci.*, **402**, 68 (2013).
33. Y. H. Tseng, H. Y. Lin, M. H. Liu, Y. F. Chen and C. Y. Mou, *J. Phys. Chem. C*, **113**, 18053 (2009).
34. F. Höffler, I. Müller and M. Steiger, *J. Chem. Thermodyn.*, **116**, 279 (2018).
35. M. J. Borah, A. Devi, R. Borah and D. Deka, *Renew. Energy*, **133**, 512 (2019).
36. Z. Muda, N. Hashim, I. M. Isa, S. A. Bakar, N. M. Ali, M. Z. Hussein, M. Mamat and S. M. Sidik, *J. Saudi Chem. Soc.*, **23**, 486 (2019).
37. Y. Khan, S. K. Durrani, M. Mehmood, J. Ahmad, M. R. Khan and S. Firdous, *Appl. Surf. Sci.*, **257**, 1756 (2010).
38. L. G. da Trindade, L. Zanchet, A. B. Trench, J. C. Souza, M. H. Carvalho, A. J. A. de Oliveira, E. C. Pereira, T. M. Mazzo and E. Longo, *Ionics (Kiel)*, **25**, 3197 (2019).
39. U. Pal, C. W. Kim, N. A. Jadhav and Y. S. Kang, *J. Phys. Chem. C*, **113**, 14676 (2009).
40. Q. Zhu, C. Xie, H. Li, C. Yang, S. Zhang and D. Zeng, *J. Mater. Chem. C*, **2**, 4566 (2014).
41. K. L. Foo, U. Hashim, K. Muhammad and C. H. Voon, *Nanoscale Res. Lett.*, **9**, 1 (2014).
42. A. J. Reddy, M. K. Kokila, H. Nagabhushana, J. L. Rao, C. Shivakumara, B. M. Nagabhushana and R. P. S. Chakradhar, *Spectrochim. Acta - Part A Mol. Biomol. Spectrosc.*, **81**, 53 (2011).
43. W. Chen, Q. Liu, S. Tian and X. Zhao, *Appl. Surf. Sci.*, **470**, 807 (2019).
44. C. I. C. Silvestre, C. Frigerio, J. L. M. Santos and J. L. F. C. Lima, *Anal. Chim. Acta*, **699**, 193 (2011).
45. J. Zhang, D. Cai, G. Zhang, C. Cai, C. Zhang, G. Qiu, K. Zheng and Z. Wu, *Appl. Clay Sci.*, **83-84**, 137 (2013).

46. Z. Shams-Ghahfarokhi and A. Nezamzadeh-Ejhieh, *Mater. Sci. Semicond. Process.*, **39**, 265 (2015).
47. S. T. Nishanthi, S. Iyyapushpam, B. Sundarakannan, E. Subramanian and D. Pathinettam Padiyan, *Appl. Surf. Sci.*, **313**, 449 (2014).
48. R. Subagyo, H. Tehubijuluw, W. Prasetyo, H. Dwi, Y. Kusumawati, H. Bahruji and D. Prasetyoko, *Arab. J. Chem.*, **15**, 103754 (2022).
49. A. A. Fauzi, A. A. Jalil, N. S. Hassan, F. F. A. Aziz, M. S. Azami, I. Hussain, R. Saravanan and D. V. N. Vo, *Chemosphere*, **286**, 131651 (2022).
50. M. S. Hamdy, H. S. M. Abd-rabboh, M. Benaissa, M. G. Al-metwaly, A. H. Galal and M. A. Ahmed, *Opt. Mater. (Amst).*, **117**, 111198 (2021).
51. M. Benaissa, N. Abbas, S. Al, N. Elboughdiri, M. G. Al-metwaly and M. A. Ahmed, *Opt. Mater. (Amst)*, **118**, 111237 (2021).
52. E. Fernandes, R. C. Martins and J. Gomes, *Sci. Total Environ.*, **718**, 137321 (2020).
53. L. Allagui, B. Chouchene, T. Gries, G. Medjahdi, E. Girot, X. Framboisier, A. B. haj Amara, L. Balan and R. Schneider, *Appl. Surf. Sci.*, **490**, 580 (2019).
54. Z. Lin, C. Du, B. Yan, C. Wang and G. Yang, *Nat. Commun.*, **9**, 1 (2018).